IEEE Access
Multidisciplinary : Rapid Review : Open Access Journal

Received April 21, 2022, accepted May 8, 2022, date of publication May 13, 2022, date of current version May 19, 2022.

Digital Object Identifier 10.1109/ACCESS.2022.3174882

Application of Convolutional Neural Network to Predict Anisotropic Effective Thermal Conductivity of Semiconductor Package

TAE-HYUN KIM[1], JEONG-HYEON PARK[2], KI WOOK JUNG[3], JAECHOON KIM[3], AND EUN-HO LEE[1,2]

[1]Department of Smart Fab. Technology, Sungkyunkwan University, Suwon, Gyeonggi-do 16419, Republic of Korea
[2]Department of Mechanical Engineering, Sungkyunkwan University, Suwon, Gyeonggi-do 16419, Republic of Korea
[3]Division of Test and System Package, Samsung Electronics, Hwaseong, Gyeonggi-do 18571, Republic of Korea

Corresponding author: Eun-Ho Lee (e.h.lee@skku.edu)

This work was supported by the Test and System Package (TSP) Division, Samsung Electronics Company Ltd.

ABSTRACT With increasing complexity of design patterns in semiconductor package substrates caused by demand for high-power semiconductors, it is necessary to be able to predict the thermal properties according to the pattern. Classifying the patterns is important to predict the effective thermal conductivity (ETC), but it has some difficulties due to the variable setting being labor-intensive and creating human uncertainty. These difficulties are amplified by the complexity of the pattern in the printed circuit board (PCB) substrate. This work presents an automated convolutional neural network (CNN)-based algorithm to infer the anisotropic ETCs of package substrates. This algorithm divides a layer-pattern image of a PCB into local unit-cell images and learns the pattern characteristics of each unit cell to identify the local ETC. The algorithm then builds an ETC map by integrating the local ETCs for the entire layer. The entire process is fully automated to reduce human uncertainty and required workforce. The ETC map from the algorithm was then used in finite element (FE) analysis and compared with three other prediction methods. The proposed algorithm can predict the anisotropic ETCs within 2–3 % errors compared to the reference data while other models lead to at least 16 % error. The FE simulation with the ETC map of the algorithm can reflect the effect of the design pattern on the heat flux and temperature distributions on the package layer, leading to the lowest root mean square error in the temperature distribution compared to other models.

INDEX TERMS Artificial intelligence, convolutional neural network, effective thermal conductivity, finite element method, semiconductor package.

I. INTRODUCTION

Semiconductor industries have attempted to predict the effective thermal conductivity (ETC) of printed circuit board (PCB) substrate [1]–[8] because heat flux affects the performance of chips while heat flows through the electrical path from heat sources [9]–[11]. Some studies have reported that the thermal energy has a significant effect on the reliability [12], [13] of systems through thermal deformation [14], dissipation [15], [16] and free energy [17] in the PCB substrate. Recent advances in heat transfer measurements have improved understanding of the aforementioned issues [18], [19]. It has been shown that, in the submicron-sized device level, the heat transfer coefficient can be significantly changed by changing the integrated materials [20], [21] and processing methods [22], [23]. Compared to material level conditions, the package substrate is more affected by the pattern design, as explained in [8], and [15]. Therefore, researches have been conducted to measure and predict the ETC at the package level in consideration of design patterns [24]. A simple approach to predict the ETC is the linear interpolation method (LIM), in which the macroscopic properties of composite materials are described based on the volume fraction of inclusions under the assumption that the inclusion builds a path parallel to the medium in the direction of heat flux [24], [27]. The LIM can be applied to semiconductor package substrates because the package substrates usually consist of copper and dielectric materials

The associate editor coordinating the review of this manuscript and approving it for publication was Agustin Leobardo Herrera-May.

This work is licensed under a Creative Commons Attribution-NonCommercial-NoDerivatives 4.0 License.
For more information, see https://creativecommons.org/licenses/by-nc-nd/4.0/

such as FR4, as shown in Fig. 1. Copper is a conductor having a high thermal conductivity and can be considered an inclusion in dielectric materials. The LIM is simple and useful for predicting the ETC along the thickness direction of the substrate. Because the thickness of the substrate layer is much thinner than the in-plane area of the substrate, the variety of patterns is limited as explained in [24], and [28]. However, the copper pattern on the plane substrate is very diverse, even for the same volume fraction. Consequently, the accuracy of the LIM for the in-plane anisotropic ETC is unsatisfactory because the LIM does not account for the difference in the thermal conductivity caused by the differences in patterns in the same volume fraction of copper. To overcome this shortcoming, some studies have proposed a method that considers the in-plane patterns in the package substrate as randomly distributed inclusions in a medium. The Maxwell-Eucken (ME) model is used for the calculation of ETC of composite materials under the assumption of dispersion of small particles within a continuous matrix of a different component. The ME considers local distortions in the temperature distributions without interfering with their neighboring distributions [26], and [29]–[32]. Another method is an effective thermal width (ETW) analysis that considers a thermal array and heat source [9], and [33]. Because the ETW accounts for the heat flux depending on the in-plane patterns of copper, it can detect the effect of heat transfer under different cases of applied power on the substrate layer. This ETW model has provided good predictions for the ETC of package substrates [24], [34], and [35], but it is not easy to accurately define the ETW in complex patterns of the substrates which is further worsened by human uncertainty. For practical consideration of the complicated patterns of the package substrate, the local characteristics of the pattern should also be considered. The piecewise simulation (PS) method divides a layer pattern into local unit cell patterns to calculate the ETCs of local areas [24], [34], and [36]. Fig. 1(b) shows examples of such unit cells from the substrate layer in Fig. 1(a). The advantage of the PS method is that it can classify unit cells by classifying the volume fraction and continuity of the patterns in each unit cell. However, if the pattern of the package substrate is very complex, leading to a significant increase in the diversity among unit cells, it is not easy to classify them, which further increases human uncertainty.

This study aims to build a fully automated algorithm to predict the in-plane anisotropic ETC of semiconductor package substrates. The presented algorithm uses a convolutional neural network (CNN) [37] to automatically extract structural feature maps of the substrate patterns. Since the CNN method is a very useful method for dealing with image data and learning features of the data [38]–[40], recent attempts have been made to solve the heat transfer [41], [42] and heat source optimization problems [43], [44] with image-based data. In this paper, based on the advantage of the CNN method, the proposed algorithm recognizes the image files of the package substrate layers as the input file and divides the entire layer into local unit cell images to learn the local ETC of the pattern. During the training of the local ETC, an image classification algorithm was used to classify the unit cell pattern. The main objective of image classification is to identify the existence of dielectric bands that block the heat flux. According to the results of the image classification, two different CNN algorithms were used, which are described in detail in Section III. For the unit cell training data, the finite element (FE) analysis data for each unit cell were used. Note that the FE analysis was also automated within the presented algorithm using a macro code. After training based on the local ETCs of each unit cell, an ETC map can be built by integrating the local ETCs for the entire layer. The entire process was fully automated. The predicted ETC results were validated by FE simulation using the original package CAD file, and three other pre-existing models were also compared to the proposed method. The methods compared are the LIM, ME, and ETW. Note that, in this paper, the compared models (LIM, ME, and ETW) were also combined with the PS method to increase the prediction accuracy by obtaining the local ETC. The results of this study show that the proposed method accurately predicts in-plane anisotropic ETCs. The remainder of this study is structured as follows. Section II briefly summarizes the three compared models (LIM, ME, and ETW), and Section III explains the proposed CNN-based algorithm in detail. Section IV presents the results and discussion, and the conclusion is presented in Section V.

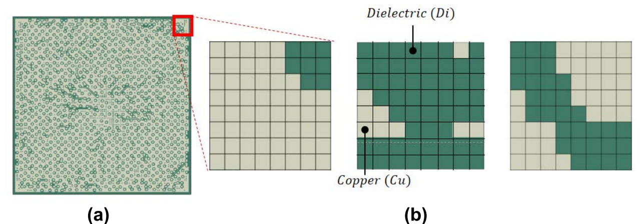

FIGURE 1. Examples of package substrates: (a) Example of one layer, and (b) Examples of unit cells.

II. SUMMARY OF THE PRE-EXISTING MODELS

This section summarizes the three pre-existing models that will be compared with the proposed method in Section IV.

A. LINEAR INTERPOLATION METHOD (LIM) MODEL

The LIM model [24]–[27] only accounts for the volume fraction of copper in the dielectric material matrix, as shown in Fig. 2(a), and the ETC of the LIM (K_{eff}^{LIM}) is defined as

$$K_{eff}^{LIM} = \phi \times K_1 + (1 - \phi) \times K_2, \tag{1}$$

where, K_1 is the thermal conductivity of copper and K_2 is the thermal conductivity of the dielectric material. ϕ denotes the volume fraction of copper. The LIM model assumes that the inclusion builds a path parallel to the medium for the direction of heat flux, and an isotropic model providing the same ETC value for all directions.

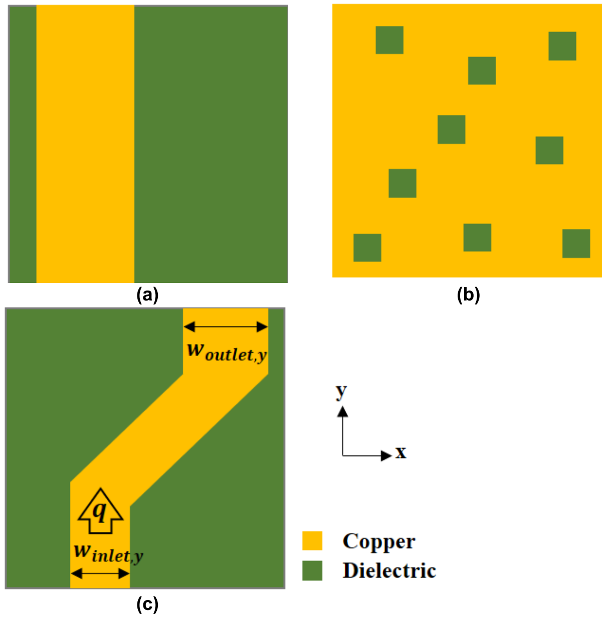

FIGURE 2. Pre-existing models: (a) LIM model, (b) ME model, and (c) ETW model.

B. MAXWELL-EUCKEN (ME) MODEL

The Maxwell-Eucken (ME) model [29]–[32] defines ETC as

$$K_{eff}^{ME} = K_1 \frac{K_2 + 2K_1 - 2(1-\phi)(K_1 - K_2)}{K_2 + 2K_1 + (1-\phi)(K_1 - K_2)}. \tag{2}$$

K_1 is the thermal conductivity usually used for continuous phase, copper substrate applied in this work, and K_2 represents the thermal conductivity of a dispersed phase such as inclusions in a composite, as shown in Fig. 2(b). ϕ denotes the volume fraction of copper. It should be noted that a random distribution of inclusions was assumed. The ME model also provided an isotropic ETC value.

C. EFFECTIVE THERMAL WIDTH (ETW) MODEL

As shown in [24], [34], and [35], the ETC changes according to the patterns and volume fraction of copper. As shown in Fig. 2(c), in the ETW model, the heat flux (Arrow-treated $\boldsymbol{q}$ in the figure) is strongly affected by the copper lines. The ETW model defines the effective width as a key variable for obtaining the ETC value, as shown in (3).

$$K_{eff,i}^{ETW} = f(w_{eff,i}), \tag{3}$$

where,

$$w_{eff,i} = \frac{w_{inlet,i} + w_{outlet,i}}{2} \quad (i = x \text{ and } y).$$

$K_{eff,i}^{ETW}$ is defined by functions of the effective width $w_{eff,i}$ and the detailed form of function $f()$ can be defined in diverse ways. The subscript i denotes the orthogonal direction of the in-plane layer to provide an anisotropic ETC. Note that Fig. 2(c) shows only the vertical direction (y-direction), but another ETW is also defined for the horizontal direction (x-direction) independently. As the effective width increases, the ETC also increases represented in Fig. 3. In Fig. 3, the reference ETC values are normalized by the thermal conductivity of the copper according to the effective width. As explained in [24], and [34], a widely used method is to use FE analysis data to build a quadratic fitting function $f()$ based on $w_{eff,i}$,. In the fitted equation in Fig. 3, x denotes the effective width and y is the fitted ETC for the ETW model. Note that, in this paper, when a pattern contains a discontinuous path of copper, the ETC is fixed as the thermal conductivity of the dielectric material.

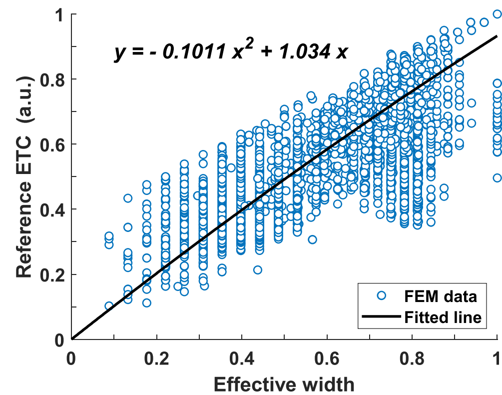

FIGURE 3. Quadratic fitting function for the ETW model.

III. PROPOSED CNN-BASED MODEL

A. IMAGE PROCESSING

Image processing is the earliest stage of the algorithm used to build the training data automatically, as shown in Fig. 4. The algorithm mainly consists of image processing, data construction, and training steps, and each step is described one by one in this Section III. This method uses the image data of the package substrate. All of the layer images provided by Samsung Electronics were standardized to 12 mm × 12.7 mm. The dimensions of the layer images have not been changed further, and one layer has 768 × 768 pixels in this work. Four-layer images were included in the substrate layout. Among the four-layer images, a one-layer image is used to compare the accuracy of several models and is called the test layer. The remaining images called the train layer are used to train the proposed CNN model. Before training, the layer images were converted to a unit cell material map through image data processing, which consisted of downsizing, and binary masking. In the downsizing process, a layer image (shown in Fig. 5(a)) was pre-processed by dividing the layer into unit cells consisting of 8 × 8 pixels, as shown in Fig. 5(b). Next, the unit cell images were converted into binary images, which had binary colors to express two-phase materials representing copper and dielectric materials, as shown in Fig. 5(c). Each color of the unit cell in Fig. 5(c) denotes copper as white, which has a thermal conductivity of 385 [W/m·K], and the dielectric material as black, which has a thermal conductivity of 0.2 [W/m·K]. For the train data, total 16,382 pieces were generated from the training layers through image processing

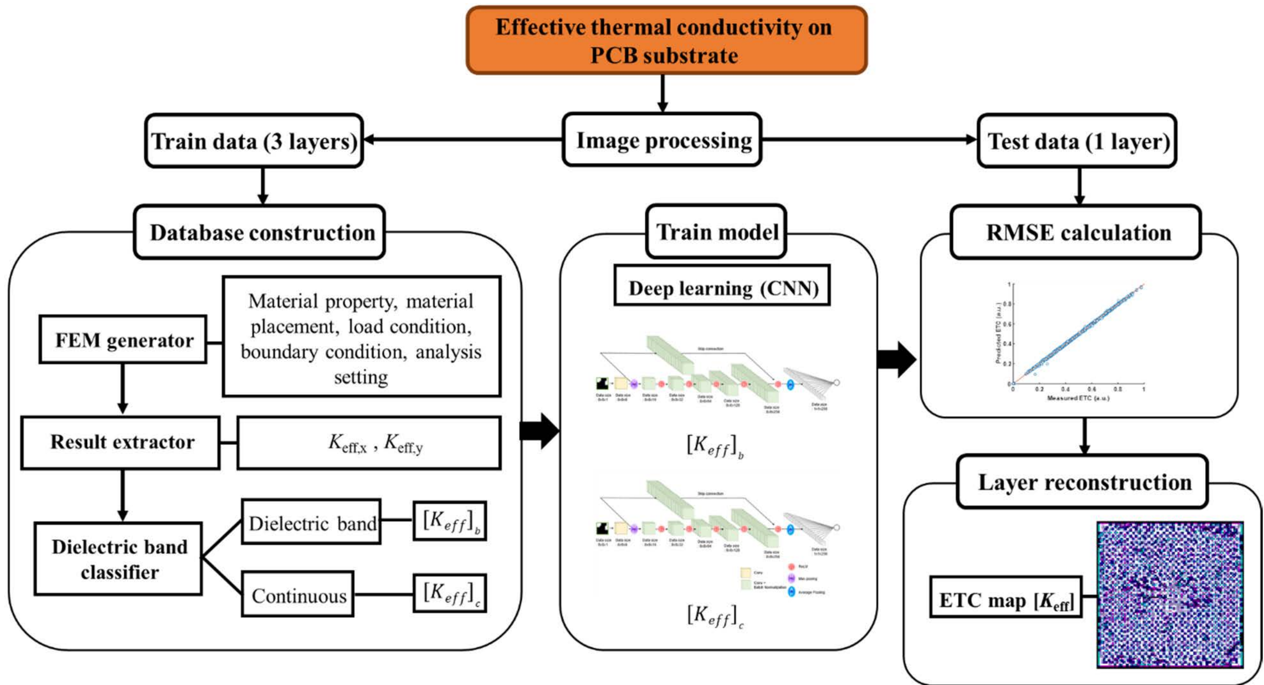

FIGURE 4. Framework of the proposed method.

after eliminating duplicated unit cell images. For the test data, 6,054 pieces were generated from test layer with the same process.

B. DATA CONSTRUCTION

To train the CNN model, the training data should be constructed from the image-processed data. The labeled unit cell ETC data were obtained by FE thermal analysis, and ABAQUS was used for heat transfer analysis. First, for the FE analysis, the unit cell images from the image processing are converted to FE mesh modeling, which is automatically generated by a mapping algorithm between the pixel and element positions in the spatial domain, as shown in Fig. 6(a).

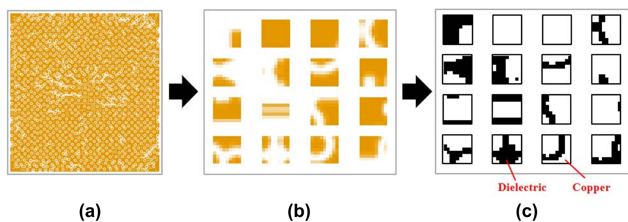

FIGURE 5. Image processing: (a) layer image, (b) downsizing, and (c) binary masking.

In this step, the FE models were created using two types of meshes, triangular and square mesh types. The effect of mesh type is discussed in Section IV. From the FE mesh modeling, two heat transfer simulations were conducted in two orthogonal directions, as shown in Fig. 6(b) and 6(c). In the simulation, the temperatures of the heat source and heat sink were fixed at 397 and 297 K, respectively. The thermal conductivities of the copper and the dielectric were 385 [W/m·K] and 0.2 [W/m·K], respectively. Then, the ETCs for the x and y-directions were extracted from the FE analysis. The ETC is calculated in the FE analysis using the conduction law [45], and [46], given as in (4),

$$\frac{q_i}{A_{cs}} = K_{eff,i}\frac{\partial T}{\partial x_i}, \quad \text{where } (i = x \text{ and } y). \tag{4}$$

q_i represents the total thermal energy per unit time applied to a unit cell in the ith direction caused by the heat source. In this study, A_{cs} denotes the cross-sectional area of the element, and $\partial T/\partial x_i$ is the temperature gradient between the heat source and sink. $K_{eff,i}$ in (4) was used for training. The total number of training data was 16,382.

After obtaining all training data, this algorithm divides the unit cell data into two groups according to the presence or absence of dielectric band, as shown in Fig. 4. The dielectric band consists of the dielectric materials resulting in blocking the copper paths and heat flux, as shown in Fig. 7 [24]. Therefore, the dielectric bands with different thermal behaviors should be considered through an image recognition algorithm that checks the connection between the lines of the material. The image recognition algorithm was conducted line-by-line, as shown in Fig. 8. It first checks the position of the copper in the first boundary line and then moves to the next line to check the connectivity of the copper included in the first and second lines. The algorithm repeats the verification process until the final line is reached. During the image recognition process from the first line to the last line, if there is an area where the dielectric connection continues, it is determined

that a dielectric band exists in the unit cell. This step is called dielectric band classifier in this work, as shown in Fig. 4.

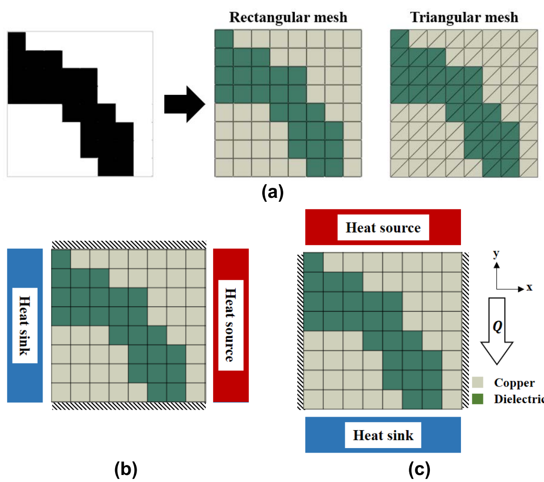

FIGURE 6. FE generator routine to build the training data: (a) FE modeling, (b) x-direction, and (c) y-direction.

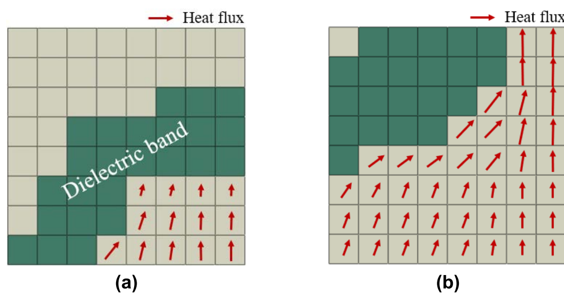

FIGURE 7. Examples of the dielectric band: (a) with band, and (b) without band.

Among 16,382 pieces of training cell images, 8,736 pieces had no dielectric band along the x-direction, and 8,010 pieces had no dielectric bands along the y-direction. They are then used to train the CNN model along the x and y-directions, separately. Note that duplicated pattern images can cause bias during training; thus, only different pattern images were extracted as the training dataset.

C. TRAINING

After the data construction state, the algorithm starts the training process. In this work, a CNN was used to predict the unit cell ETC because it has shown excellent performance in image training [47], and [48]. The CNN structure is shown in Fig. 9. A skip connection, which has shown good performance in image detection using a shortcut path connecting the starting and end parts [49], was used. The kernel size of the convolutional layer was fixed at 3 × 3, and the stride size was 1. Whenever the data passes through the convolutional layer, the number of kernels increased from 8 to 256. Zero padding was applied to maintain the data size. During the training process, a batch normalization layer was used to prevent data biasing. The ReLU function was used as an activation function to increase the nonlinearity of the network and construct a deeper network system. The max-pooling layer was introduced to decrease the complexity of the network and prevent overfitting. A fully connected layer before the output regression layer was used to integrate the parameters collected by the previous layers and output one value related to the ETC.

In this study, identical CNN model structures and training methods were used in each x and y direction. In the learning process, the Adam optimizer was used to minimize RMSE, as shown in (5).

$$RMSE = \sqrt{\sum_{i=1}^{n} \frac{(y_i - \hat{y}_i)^2}{n}} \tag{5}$$

where y_i is the ETC obtained from the FE analysis while $\hat{y}_i$ is the predicted ETC ($i = 1, 2, 3, \ldots, n$). n is the total number of validation data points. As a training option, the learning rate was 0.001, the number of epochs was 200, and the mini-batch size was 128.

IV. RESULTS AND DISCUSSIONS

A. PERFORMANCE OF THE PROPOSED MODEL

After the training of the model, the quality of the prediction was verified with the test data. The test dataset comprised of about 27 % of the whole dataset, which contained 6,054 unit cells. The predicted ETC values show good agreements with the test data (reference ETC), as shown in Fig. 10. The value of R^2 measure is 0.9998 in both x and y-directions. Note that the ETC is expressed with normalized values between zero and one. Although the test layer data were not used in the training process, the proposed model predicted well. Therefore, a high-quality prediction can be expected with other new layers for further practical applications.

Fig. 10 presents the predicted results by the trained model based on the rectangular mesh FE model. In order to analyze the effect of mesh type, as shown in Fig. 6(a), the differences of $K_{eff,x}$ and $K_{eff,y}$ between two different mesh types are compared. In case of $K_{eff,x}$, the two mesh types of 6,054 unit cells lead to 13.63 [W/m·K] in the maximum difference, 0.0 [W/m·K] in the minimum difference, and 1.33 [W/m·K] in the average. The maximum difference and average value are about 3.5% and 0.3% compared to the heat transfer coefficient of the copper (385 [W/m·K]), which is the main material for conduction in this work. The maximum, minimum, and average of the differences in $K_{eff,y}$ are 8.49 [W/m·K], 0.0 [W/m·K], and 1.25 [W/m·K], respectively. Changing the mesh type does not significantly affect the results of the simple heat transfer analysis. Based on these results, all subsequent studies are conducted using the results from the rectangular mesh type because the rectangular mesh type can reduce the number of elements.

Fig. 11, the effect of the dielectric band classifier in the y-direction is discussed with absolute percentile

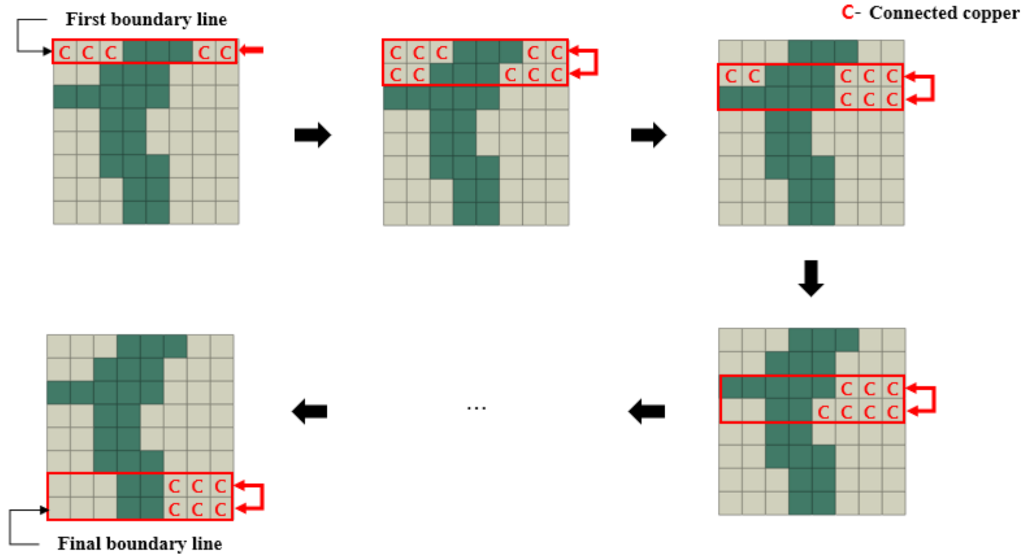

FIGURE 8. Image recognition algorithm checking the connectivity of copper.

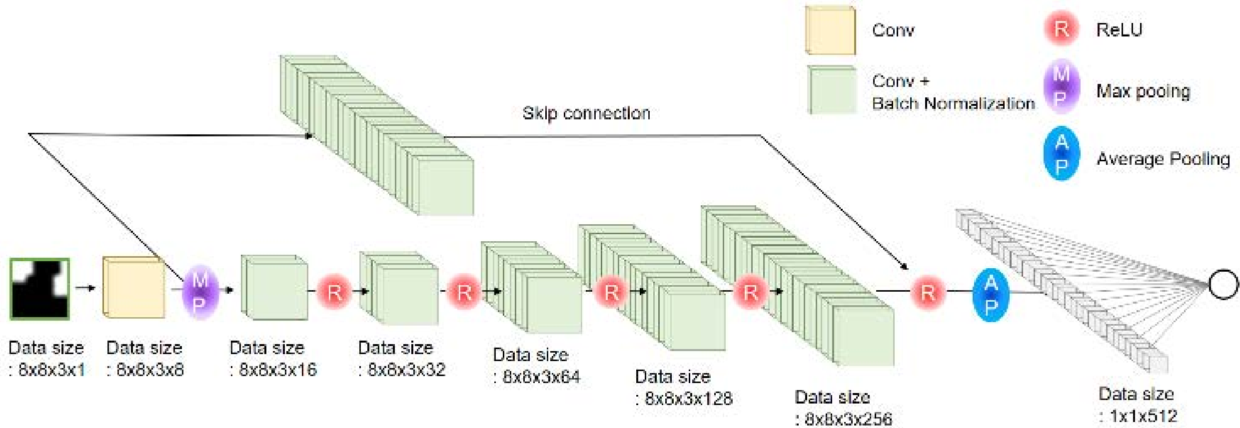

FIGURE 9. Structure of the CNN model.

error (APE), defined by

$$APE = \left| \frac{y_i - \hat{y}_i}{y_i} \right|, \quad \text{where } i = 1, 2, 3, \ldots, n. \tag{6}$$

y_i denotes the reference ETC and $\hat{y}_i$ denotes the estimated unit cell ETC. By using APE, the effect of improving accuracy through the dielectric band classifier can be checked especially in the low range of reference ETC. Fig. 11(a) presents the case without the dielectric band classifier while Fig. 11(b) shows the opposite results with the dielectric band classifier. The reference ETC is normalized by thermal conductivity of the copper. While the APE range in Fig. 11(a) is from 0 to 10, the range of Fig. 11(b) is below 0.3. The distribution of the APE is also expressed as root mean square percentile error (RMSPE), as shown in (7).

$$RMSPE = \sqrt{\frac{1}{n} \sum_{i=1}^{n} \left(\frac{y_i - \hat{y}_i}{y_i} \right)^2}. \tag{7}$$

The case without the dielectric band classifier produces a larger RMSPE result compared to the case with dielectric band classifier, corresponding to 0.3725 and 0.0008, respectively. This comparison confirms the important role of the dielectric band classifier in the algorithm.

The ETC values predicted by the CNN-based model are analyzed (blue dots in Fig. 12) along the y-direction based on the viewpoint of the volume fraction of copper and effective thermal width from the results in Fig. 10. Fig. 12(a) presents the ETC predicted by the CNN-based model according to the volume fraction, consisting of copper paths. The proposed model shows that even the same volume fraction results in different ETC values, meaning that the volume fraction alone cannot provide sufficient information to predict the ETC. However, the LIM and ME models only provide simplified values from the fitted curve. The orange line and yellow curve denote the LIM and ME models, respectively (refer to (1) and (2)). Fig. 12(b) presents the pattern effect based on the effective width and demonstrates that the ETCs from

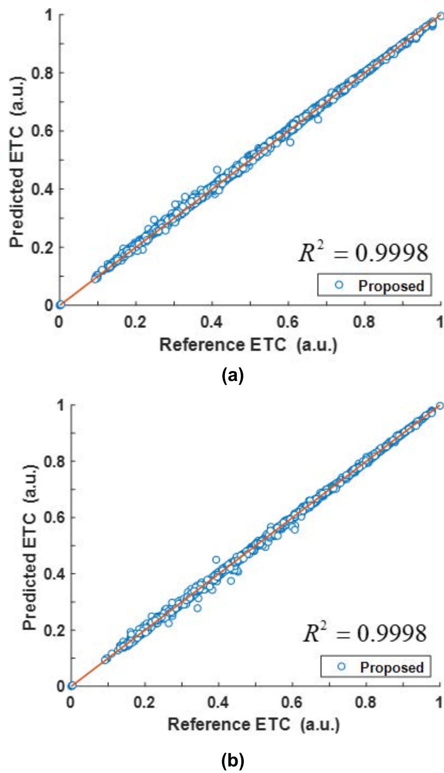

FIGURE 10. Comparison between the reference and predicted ETC of test data: (a) x-direction, and (b) y-direction.

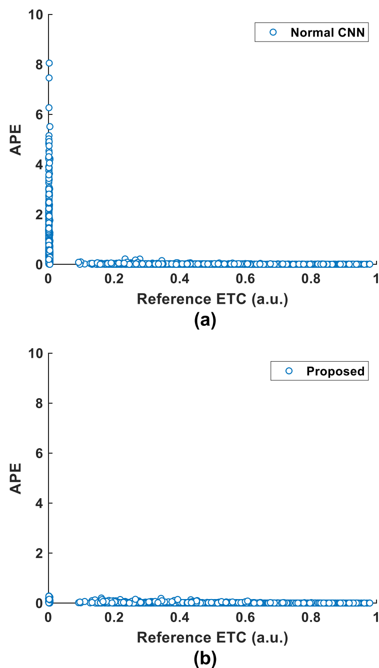

FIGURE 11. APE for the test dataset according to the dielectric band classifier in the y-direction: (a) without dielectric band classifier, and (b) with dielectric band classifier.

the CNN-based model are different even under the same effective thermal width. Among the pre-existing models for the comparison, only the ETW model (the orange curve in Fig. 12(b)) can account for the effective width. As shown in Fig. 12, the proposed CNN-based model is more flexible when considering the diversity of the data.

Fig. 13 compares the proposed model with three other pre-existing models for the accuracy of the prediction. In Fig. 13, the value on the vertical axis indicates the normalized value of the difference between the predicted and reference ETC values. In most cases, as the volume fraction increased, the difference gradually increased. The proposed CNN-based model showed significantly better results for all volume fractions.

In the case of the ETW model, the data are located at both negative and positive values, meaning that there exist all cases where the predicted ETC is greater than or lower than the reference data. This is because even though some unit cells have the same effective width, their reference ETCs can be distributed over a wider range. The LIM and ME models show the largest errors because they only account for the volume fraction of copper, without considering the dielectric band effect.

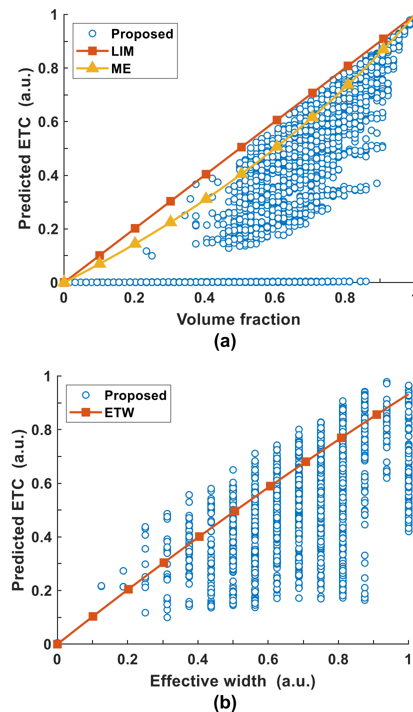

FIGURE 12. Predicted ETC of unit cells according to volume fraction and effective width along the y-direction: (a) ETC according to volume fraction, and (b) ETC according to the effective width.

Among the results in Fig. 13, a representative case of unit cell is shown in Fig. 14, and the ETC results of the models are summarized in Table 1. There is a dielectric band protecting heat flux along the y-direction in the unit cell. The predicted ETC values of the LIM and ME models were much higher than those of the other models, while the other models provided much smaller ETCs because of the dielectric band. The proposed model provides a good prediction. The detailed reasons for the result are shown in Fig. 13. For quantitative

comparison with Fig. 13, RMSE was calculated as shown in Table 2. The LIM and ME models presented the highest values because of their simplicity, and the proposed method provided the lowest error than the other methods.

TABLE 1. Comparison of ETC for the unit cell along the y-Direction.

Model	ETC [W/m·K]
Reference	0.61
Proposed	0.63
LIM	234.69
ME	168.87
ETW	0.20

TABLE 2. Comparison of RMSE for unit cell ETCs.

Model	x-direction [W/m·K]	y-direction [W/m·K]
Proposed	1.74	1.47
LIM	142.22	150.18
ME	114.01	121.58
ETW	49.47	48.67

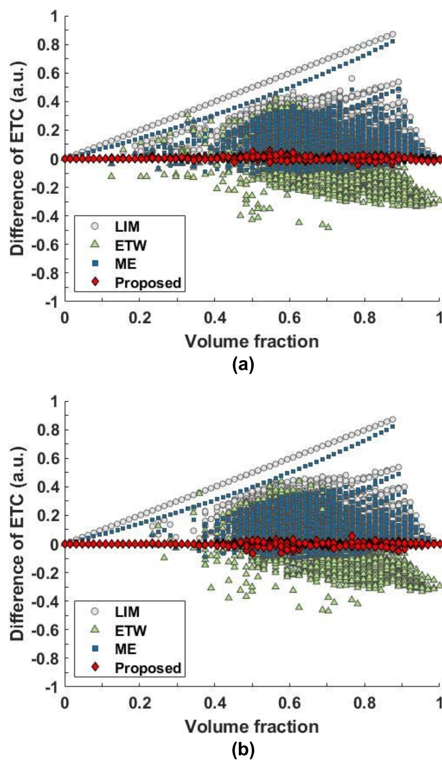

FIGURE 13. Comparison of the proposed model to other three models. (a) x-direction, and (b) y-direction.

B. DISCUSSIONS

A well-predicted ETC of a unit cell is required to obtain high prediction accuracy in layer-scale thermal simulations, which

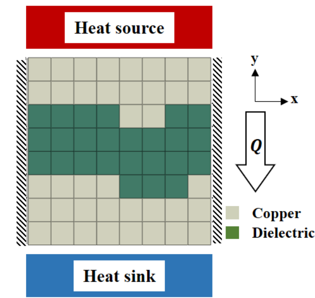

FIGURE 14. An example of unit cell having a dielectric band.

is used in practical applications. The CNN-based model's ETC prediction values in the x and y-directions were used in-plane anisotropic thermal conductivity. The ETC in the thickness direction (z-direction) is related to the volume fraction because the volume fraction-based ETC model provides good results in the thickness direction [24]; thus, can be calculated analytically using (1). The orthotropic ETCs can be mapped to the RGB color palette with ETC in the x-direction being red, in the y-direction being green, and in the z-direction being blue, which makes it convenient to compare the distribution of ETCs. The ETC maps of test layer from the proposed model and pre-existing models are shown in Fig. 15. The converted images from LIM and ME models are expressed as grayscale images because they are isotropic. In contrast, the proposed and ETW models have RGB coloring because they reflect anisotropy. The ETC map in Fig. 15 can be used for heat-transfer simulations.

Next, using the ETC maps shown in Fig. 15, steady-state thermal analysis was conducted for the x and y-directions. The same boundary condition was applied, as shown in Fig. 6. The temperatures of the heat source and sink were 397 and 297 K, respectively. The results of the temperature distributions are presented in Fig. 16 and 17, and RMSE of the temperature distribution on the layer was calculated, as shown in Table 3. Note that the FE reference refers to the FE simulation result with the original package CAD file, and it was used as a reference. Therefore, the FE model does not have the ETC map; the unit cells and ETC map were created in the models to learn the effect of the local pattern. The temperature contour of the proposed model is in good agreement with the contour of the FE reference. Among the pre-existing models, the ETW also shows a similar temperature contour to the FE reference model. The proposed and ETW models present bumpy temperature boundaries because of the dielectric bands. The dielectric bands build an obstacle to the heat flow and divert the heat flow. On the other hand, the LIM and ME models show that the border lines of the temperature are parallel, in Fig. 16 and 17, because they do not consider the dielectric band, which results in relatively simple heat flow. The details are discussed in Fig. 18.

In Table 3, RMSEs of the proposed model provide the lowest errors among the presented models. Fig. 18 shows the magnitudes of the heat flux vectors on the layer. The proposed

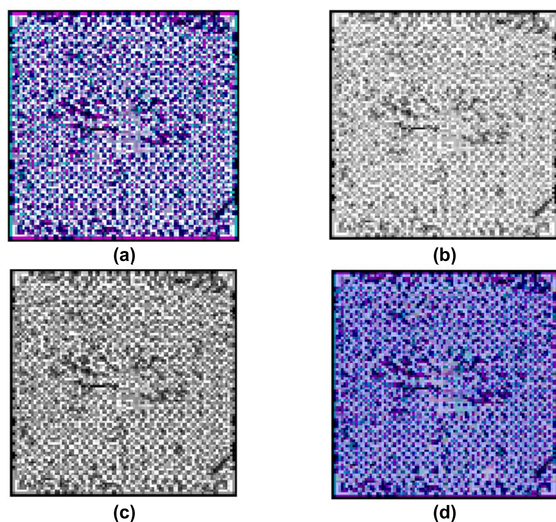

FIGURE 15. Comparison of the test layer ETC maps: (a) Proposed model, (b) LIM model, (c) ME model, and (d) ETW model.

TABLE 3. Temperature RMSE in the x and y-directions.

Model	x-direction [K]	y-direction [K]
Proposed	1.43	1.54
LIM	1.95	2.95
ME	1.90	2.54
ETW	1.76	1.71

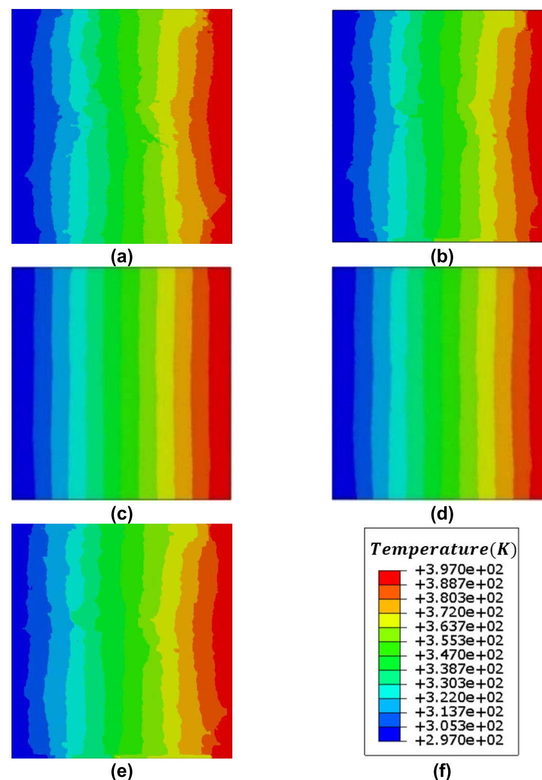

FIGURE 16. Temperature distribution of the test layer under the boundary condition of x-direction: (a) FE reference, (b) Proposed model, (c) LIM model, (d) ME model, (e) ETW model, and (f) Range of temperature.

and ETW models show similar distribution compared to the FE reference, whereas the LIM and ME models have very uniform heat flux distributions throughout the layer. This is why the temperature contours of the LIM and ME models present parallel border lines in Fig. 16 and 17. Based on the heat transfer simulation shown in Fig. 16–18, the thermal properties including thermal resistance, layer ETC, and average heat flux of the entire layer were calculated, shown in Table 4. The average heat flux was obtained with dividing the sum of the heat flux magnitudes of all elements by the number of elements for each direction. By using the thickness of a layer (10 μm), the thermal resistance R was calculated dividing the difference between the boundary temperatures by the heat transfer rate. The ETC value representing the entire layer (layer ETC in Table 4) can be calculated using (4) based on the average heat flux of the layer.

The thermal properties of each model in Table 4 are compared to the reference data. The proposed model results in errors of 2.00 % and 1.96% in the thermal resistance and the layer ETC, respectively, along the x-direction. The ETW model leads to errors of 19.24 % and 16.14 % in the thermal resistance and the layer ETC along the same direction. In the y-direction, the proposed model gives 2.9 % and 2.3 % errors for the thermal resistance and the layer ETC, respectively, while the ETW model results in 19.9 % and 16.6 % errors for the same properties. For the average magnitude of heat flux, the proposed and ETW models lead to 1.96 % and 16.6 %, respectively. These results show that the proposed model leads to closer results to the FE reference data than the ETW model. Note that both models (the proposed and ETW) show much higher accuracy compared to the other models. For example, the LIM and ME models have 96.85 % and 74.85 % errors, respectively, for the layer ETC along the x-direction.

For a new FE simulation, Fig. 19 presents another boundary condition with four heat sources. The heat sources are placed symmetrically with respect to the center. The temperatures of heat sources and sinks are 397 and 297 K, respectively. Fig. 20 show the results of the four models. While the LIM and ME models show symmetric temperature distributions, the proposed and ETW models show some asymmetries. This is because the proposed and ETW models reflect the characteristics of the local pattern, and they exhibit temperature distributions similar to that of the FE reference.

For a more detailed comparison, the temperature distribution along the line of A-A' is presented in Fig. 21. As shown in Fig. 21(a), the FE reference (blue line) shows the asymmetric temperature distribution due to the different local design patterns. The proposed and ETW models can follow the asymmetric distribution, on the other hand, the LIM and ME models provide symmetrical temperature distributions. The main position of the temperature asymmetry is marked with

TABLE 4. Comparison of thermal properties of the whole layer along the x and y-directions.

Model	x-direction			y-direction		
	R [K/W]	Layer ETC [W/m·K]	Average heat flux [kW/m^2]	R [K/W]	Layer ETC [W/m·K]	Average heat flux [kW/m^2]
Reference	700.46	129.27	1124.12	855.46	118.56	974.14
Proposed	714.47	126.74	1102.08	880.15	115.23	946.80
LIM	355.84	254.47	2212.80	400.74	253.09	2079.49
ME	400.62	226.03	1965.48	451.61	224.58	1845.24
ETW	835.24	108.41	942.73	1025.85	98.87	812.34

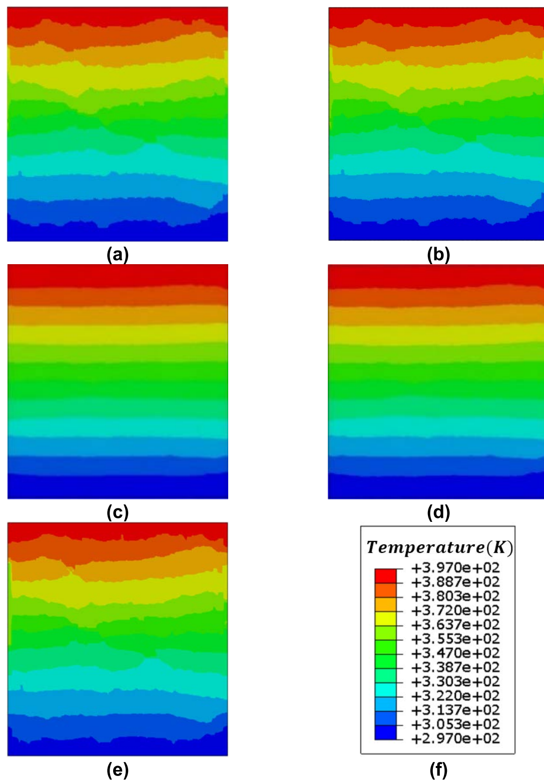

FIGURE 17. Temperature distribution of the test layer under the boundary condition of y-direction: (a) FE reference, (b) Proposed model, (c) LIM model, (d) ME model, (e) ETW model, and (f) Range of temperature.

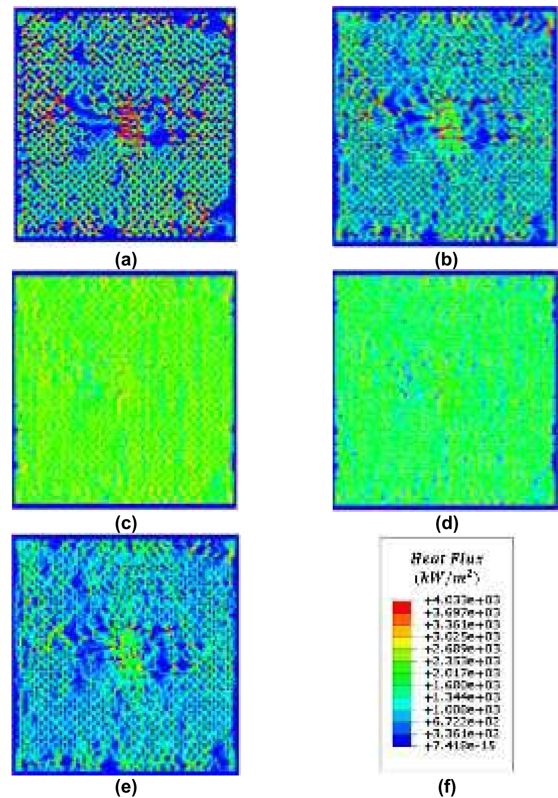

FIGURE 18. Heat flux magnitude distribution of the test layer under the boundary condition of y-direction: (a) FE reference, (b) Proposed model, (c) LIM model, (d) ME model, (e) ETW model, and (f) Range of heat flux.

a red dotted square on the line A-A' line in the lower part of Fig. 21(a); the temperature field image in Fig. 21(a) is from the proposed model.

Fig. 21(b) and 21(c) magnify the temperature fields in the inner area of the red dotted square from the temperature results of the proposed and LIM models, respectively. The proposed model and the LIM model represent the difference according to whether the pattern design is learned or not.

Finally, Fig. 22(a) and 22(b) compare the heat flux results of the new model and LIM model, respectively, in nine unit cells inside the blue square positioned at the center of Fig. 21(b) and 21(c). The binary colors in the background of Fig. 22(a) and 22(b) show the pattern design from the binary

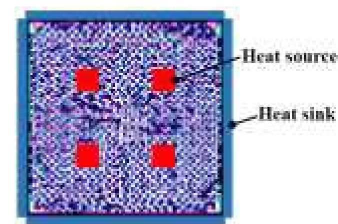

FIGURE 19. Boundary condition of ETC map on the test layer for the example with four heat sources.

images of the unit cells, as shown in Fig. 5. The arrows are the heat flux vectors and the numbers indicate the magnitude

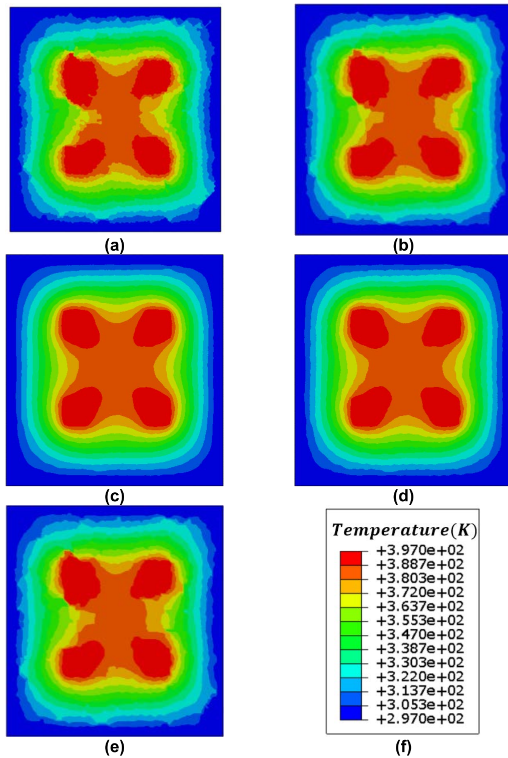

FIGURE 20. Heat transfer simulation of the test layer with four heat sources: (a) FE reference, (b) Proposed model, (c) LIM model, (d) ME model, (e) ETW model, and (f) Range of temperature.

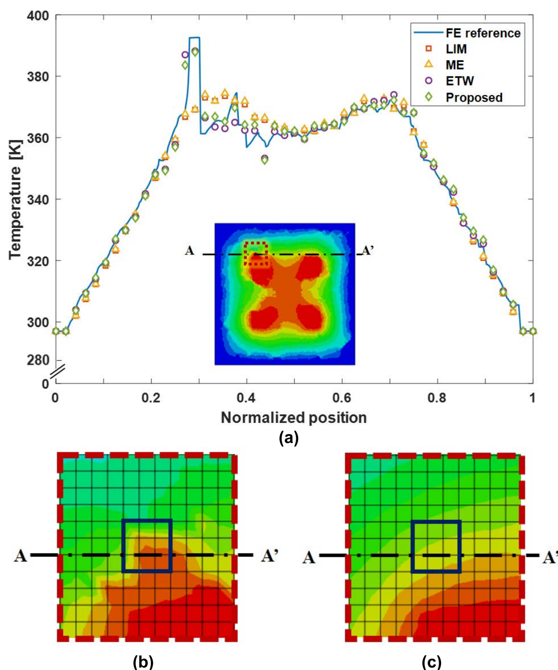

FIGURE 21. Temperature analysis along the A-A′ line: (a) Temperature distribution curve, (b) Inner area of the red dotted square from the proposed model, and (c) Inner area of the red dotted square from the LIM model.

of the vector. In Fig. 22(a), it can be seen that the heat flux is significantly lowered at the positions where the dielectric

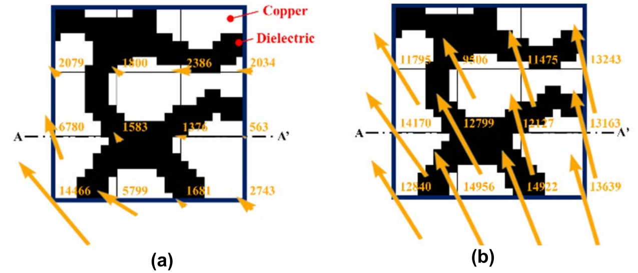

FIGURE 22. Heat flux analysis near the asymmetric temperature field region: (a) heat flux of proposed model (unit: kW/m^2), and (b) heat flux of LIM model (unit: kW/m^2).

FIGURE 23. Interface of the automated ETC prediction program

bands exist, whereas the LIM model, in Fig. 22(b), does not consider the dielectric pattern.

The results of this paper show that the proposed algorithm can predict the anisotropic ETC of the package substrate with very high accuracy. The ETC in a semiconductor affects not only the temperature distribution inside the semiconductor but also the temperature distribution of the entire electronic device system because semiconductors are the main heat sources in electronic devices [43], [44]. Therefore, the ETC map provided by this algorithm can be used as important information to improve the thermal management quality of the entire electronic device system [50]–[52]. Furthermore, the CNN-based algorithm in this paper not only predicts the ETC with high accuracy, but is also fully automated to greatly reduce human labor time. Fig. 23 shows the interface of the automated prediction program. By clicking the buttons in Fig. 23, the whole process processes are completed automatically, greatly reducing the labor-intensive tasks. In addition, from a long-term perspective, this algorithm has a potential to develop into an advanced technology that can propose a package design considering the thermal distribution as well as the electronic performance.

V. CONCLUSION

This paper presents an application of CNN-based prediction of the ETC for semiconductor package substrates. The results are summarized as follows.

1. The proposed CNN-based algorithm divides a layer-pattern image of a PCB into local unit-cell images and learns the pattern characteristics of each unit cell to identify the local ETC. The algorithm then builds an ETC map for a PCB layer by integrating the local ETC of the unit cells to use in thermal analyses.

2. The CNN-based algorithm is fully automated and does not need to define arbitrary functions or variables, thus reducing human uncertainty and labor intensity.

3. The proposed model was validated by FE simulation using the original package-layer CAD file. The results of the model were in good agreement with the results of the FE simulation for the temperature contour and heat fluxes.

4. Considering the dielectric band is very important to increase the prediction accuracy because it strongly blocks the heat flux. The proposed model builds the dielectric band classifier, and it shows good performance.

5. The proposed model shows a comparative advantage over other models in accuracy and convenience.

ACKNOWLEDGMENT

(Tae-Hyun Kim and Jeong-Hyeon Park are co-first authors.)

REFERENCES

[1] S. Krishnan, S. V. Garimella, G. M. Chrysler, and R. V. Mahajan, ''Towards a thermal Moore's law,'' *IEEE Trans. Adv. Packag.*, vol. 30, no. 3, pp. 462–474, Aug. 2007.

[2] F. Kohl, R. Fasching, F. Keplinger, R. Chabicovsky, A. Jachimowicz, and G. Urban, ''Development of miniaturized semiconductor flow sensors,'' *Measurement*, vol. 33, no. 2, pp. 109–119, 2003.

[3] Y. Ning, M. H. Azarian, and M. Pecht, ''Effects of voiding on thermomechanical reliability of copper-filled microvias: Modeling and simulation,'' *IEEE Trans. Device Mater. Rel.*, vol. 15, no. 4, pp. 500–510, Dec. 2015.

[4] M. Soltani, R. Kulkarni, T. Scheinost, T. Groezinger, and A. Zimmermann, ''A novel approach for reliability investigation of LEDs on molded interconnect devices based on FE-analysis coupled to injection molding simulation,'' *IEEE Access*, vol. 7, pp. 56163–56173, 2019.

[5] M. Akbari, M. T. Bina, A. S. Bahman, B. Eskandari, E. Pouresmaeil, and F. Blaabjerg, ''An extended multilayer thermal model for multichip IGBT modules considering thermal aging,'' *IEEE Access*, vol. 9, pp. 84217–84230, 2021.

[6] J. Zhao, F. Deng, W. Hu, Y. Du, and S. Abulanwar, ''Thermal optimization strategy based on second-order harmonic circulating current injection for MMCs,'' *IEEE Access*, vol. 9, pp. 80183–80196, 2021.

[7] Y. Shen, H. Wang, F. Blaabjerg, H. Zhao, and T. Long, ''Thermal modeling and design optimization of PCB vias and pads,'' *IEEE Trans. Power Electron.*, vol. 35, no. 1, pp. 882–900, Jan. 2020.

[8] J. Chai, G. Dong, and Y. Yang, ''An effective approach for thermal performance analysis of 3-D integrated circuits with through-silicon vias,'' *IEEE Trans. Compon., Package. Manuf. Technol.*, vol. 9, no. 5, pp. 877–887, May 2019.

[9] D. S. Gautam, F. Musavi, D. Wager, and M. Edington, ''A comparison of thermal vias patterns used for thermal management in power converter,'' in *Proc. IEEE Energy Convers. Congr. Expo.*, Sep. 2013, pp. 2214–2218.

[10] C. Yu, C. Buttay, and E. Laboure, ''Thermal management and electromagnetic analysis for GaN devices packaging on DBC substrate,'' *IEEE Trans. Power Electron.*, vol. 32, no. 2, pp. 906–910, Feb. 2016.

[11] A. Wileman, S. Perinpanayagam, and S. Aslam, ''Physics of failure (PoF) based lifetime prediction of power electronics at the printed circuit board level,'' *Appl. Sci.*, vol. 11, no. 6, p. 2679, Mar. 2021.

[12] M. Soltani, M. Freyburger, R. Kulkarni, R. Mohr, T. Groezinger, and A. Zimmermann, ''Reliability study and thermal performance of LEDs on molded interconnect devices (MID) and PCB,'' *IEEE Access*, vol. 6, pp. 51669–51679, 2018.

[13] Y. Zhang, ''Improved numerical-analytical thermal modeling method of the PCB with considering radiation heat transfer and calculation of components' temperature,'' *IEEE Access*, vol. 9, pp. 92925–92940, 2021.

[14] M.-C. Liao, P.-S. Huang, Y.-H. Lin, M.-Y. Tsai, C.-Y. Huang, and T.-C. Huang, ''Measurements of thermally-induced curvatures and warpages of printed circuit board during a solder reflow process using strain gauges,'' *Appl. Sci.*, vol. 7, no. 7, p. 739, Jul. 2017.

[15] F. Ghioldi, J. Hélie, and F. Piscaglia, ''A fast computational method for the optimal thermal design of anisotropic multilayer structures with discrete heat sources for electrified propulsion systems,'' *Int. J. Heat Mass Transf.*, vol. 183, Feb. 2022, Art. no. 122114.

[16] E.-H. Lee and W. Choi, ''Asymptotic profile of solutions to the heat equation on thin plate with boundary heating,'' *Appl. Math. Comput.*, vol. 408, Nov. 2021, Art. no. 126356.

[17] E.-H. Lee, ''A model for irreversible deformation phenomena driven by hydrostatic stress, deviatoric stress and an externally applied field,'' *Int. J. Eng. Sci.*, vol. 169, Dec. 2021, Art. no. 103573.

[18] J. Park, K. Bae, T. R. Kim, C. Perez, A. Sood, M. Asheghi, K. E. Goodson, and W. Park, ''Direct quantification of heat generation due to inelastic scattering of electrons using a nanocalorimeter,'' *Adv. Sci.*, vol. 8, no. 3, Feb. 2021, Art. no. 2002876.

[19] S. Chaikasetsin, T. Kodama, K. Bae, J. Y. Jung, J. Shin, B. C. Lee, B. S. Y. Kim, J. Seo, U. Sim, F. B. Prinz, K. E. Goodson, and W. Park, ''Thermal expansion characterization of thin films using harmonic Joule heating combined with atomic force microscopy,'' *Appl. Phys. Lett.*, vol. 118, no. 19, May 2021, Art. no. 194101.

[20] T. Kim, S. I. Park, C. Song, H. Lee, and J. Cho, ''Fundamental conduction cooling limits for sub-1 μm Ga_2O_3 devices integrated with diamond,'' *Int. J. Heat Mass Transf.*, vol. 191, Aug. 2022, Art. no. 122864.

[21] T. Kim, S. Kim, E. Kim, T. Kim, J. Cho, C. Song, and S. Baik, ''High-temperature skin softening materials overcoming the trade-off between thermal conductivity and thermal contact resistance,'' *Small*, vol. 17, no. 38, Sep. 2021, Art. no. 2102128.

[22] J. Kim, S. Lee, Y. Song, S. Choi, J. An, and J. Cho, ''Thermal conductivity of plasma-enhanced atomic layer deposited hafnium zirconium oxide dielectric thin films,'' *J. Eur. Ceram. Soc.*, vol. 41, no. 6, pp. 3397–3403, Jun. 2021.

[23] J. Cho, J. Park, F. B. Prinz, and J. An, ''Thermal conductivity of ultrathin $BaTiO_3$ films grown by plasma-assisted atomic layer deposition,'' *Scripta Mater.*, vol. 154, pp. 225–229, Sep. 2018.

[24] S. Hwang, B. W. Lee, T. Kim, Y. Hyun, H. Hwang, S. Ryu, M. Choi, Y. Kim, and D. S. Oh, ''Effective substrate thermal conductivity modeling method extracted from detailed pattern for premium SOC packages,'' in *Proc. 19th IEEE Intersociety Conf. Thermal Thermomechanical Phenomena Electron. Syst. (ITherm)*, Jul. 2020, pp. 244–248.

[25] D. Kumlutas and I. H. Tavman, ''A numerical and experimental study on thermal conductivity of particle filled polymer composites,'' *J. Thermoplastic Compos. Mater.*, vol. 19, no. 4, pp. 441–455, Jul. 2006.

[26] J. Wang, J. K. Carson, M. F. North, and D. J. Cleland, ''A new approach to modelling the effective thermal conductivity of heterogeneous materials,'' *Int. J. Heat Mass Transf.*, vol. 49, pp. 3075–3083, Aug. 2006.

[27] J. K. Carson, S. J. Lovatt, D. J. Tanner, and A. C. Cleland, ''Thermal conductivity bounds for isotropic, porous materials,'' *Int. J. Heat Mass Transf.*, vol. 48, no. 11, pp. 2150–2158, May 2005.

[28] S. Bensebaa, M. Berkani, S. Lefebvre, M. Petit, and N. Schmitt, ''Experimental and numerical characterization of PCB-embedded power dies using solderless pressed metal foam,'' in *Proc. 22nd Eur. Conf. Power Electron. Appl. (EPE ECCE Europe)*, Sep. 2020, pp. 1–10.

[29] A. Eucken, ''Allgemeine gesetzmäßigkeiten für das Wärmeleitvermögen verschiedener stoffarten und aggregatzustände,'' *Forschung auf dem Gebiete des Ingenieurwesens*, vol. 11, no. 1, pp. 6–20, Jan. 1940.

[30] J. C. Maxwell, ''Conduction through heterogeneous media,'' in *A Treatise on Electricity and Magnetism*, 3rd ed. New York, NY, USA: Dover, 1954, ch. 9.

[31] R. P. A. Rocha and M. A. E. Cruz, ''Computation of the effective conductivity of unidirectional fibrous composites with an interfacial thermal resistance,'' *Numer. Heat Transfer, Appl.*, vol. 39, no. 2, pp. 179–203, Feb. 2001.

[32] G. B. A. Carotenuto, "The effective thermal conductivity of packed beds of spheres for a finite area," *Numer. Heat Transf. A, Appl.*, vol. 37, no. 4, pp. 343–357, Mar. 2000.

[33] S. P. Gurrum, M. D. Romig, S. J. Horton, and D. R. Edwards, "A quick PCB thermal calculator to aid system design of exposed pad packages," in *Proc. 27th Annu. IEEE Semiconductor Thermal Meas. Manage. Symp.*, Mar. 2011, pp. 1–8.

[34] Y. Cho, Y. Hyun, Y. Im, and Y. Shin, "Pattern continuity check approach to model effective thermal conductivity of PCB," in *Proc. 19th IEEE Intersociety Conf. Thermal Thermomechanical Phenomena Electron. Syst. (ITherm)*, Jul. 2020, pp. 909–917.

[35] J. R. Culham and M. M. Yovanovich, "Factors affecting the calculation of effective conductivity in printed circuit boards [thermal analysis]," in *Proc. 6th Intersociety Conf. Thermal Thermomechanical Phenomena Electron. Syst.*, 1998, pp. 460–467.

[36] B. Blackmore, "Validation and sensitivity analysis of an image processing technique to derive thermal conductivity variation within a printed circuit board," in *Proc. 25th Annu. IEEE Semiconductor Thermal Meas. Manage. Symp.*, Mar. 2009, pp. 76–86.

[37] S. Albawi, T. A. Mohammed, and S. Al-Zawi, "Understanding of a convolutional neural network," in *Proc. Int. Conf. Eng. Technol. (ICET)*, Aug. 2017, pp. 1–6.

[38] A. Dhillon and G. K. Verma, "Convolutional neural network: A review of models, methodologies and applications to object detection," *Prog. Artif. Intell.*, vol. 9, no. 2, pp. 85–112, 2020.

[39] A. Kumar, G. Vashishtha, C. P. Gandhi, Y. Zhou, A. Glowacz, and J. Xiang, "Novel convolutional neural network (NCNN) for the diagnosis of bearing defects in rotary machinery," *IEEE Trans. Instrum. Meas.*, vol. 70, pp. 1–10, 2021.

[40] T. Hur, L. Kim, and D. K. Park, "Quantum convolutional neural network for classical data classification," *Quantum Mach. Intell.*, vol. 4, no. 1, pp. 1–18, Jun. 2022.

[41] Y. Suh, R. Bostanabad, and Y. Won, "Deep learning predicts boiling heat transfer," *Sci. Rep.*, vol. 11, no. 1, pp. 1–10, Dec. 2021.

[42] T. Liu, Y. Li, Q. Jing, Y. Xie, and D. Zhang, "Supervised learning method for the physical field reconstruction in a nanofluid heat transfer problem," *Int. J. Heat Mass Transf.*, vol. 165, Feb. 2021, Art. no. 120684.

[43] J. Sun, J. Zhang, X. Zhang, and W. Zhou, "A deep learning-based method for heat source layout inverse design," *IEEE Access*, vol. 8, pp. 140038–140053, 2020.

[44] C. Qian, R. K. Tan, and W. Ye, "An adaptive artificial neural network-based generative design method for layout designs," *Int. J. Heat Mass Transf.*, vol. 184, Mar. 2022, Art. no. 122313.

[45] Y. C. Hua and B. Y. Cao, "The effective thermal conductivity of ballistic-diffusive heat conduction in nanostructures with internal heat source," *Int. J. Heat Mass Transf.*, vol. 92, pp. 995–1003, 2016.

[46] E.-H. Lee, D.-Y. Yang, and W.-H. Yang, "Numerical modeling and experimental validation of focused surface heating using near-infrared rays with an elliptical reflector," *Int. J. Heat Mass Transf.*, vol. 78, pp. 240–250, Nov. 2014.

[47] J. Wan, J.-W. Jiang, and H. S. Park, "Machine learning-based design of porous graphene with low thermal conductivity," *Carbon*, vol. 157, pp. 262–269, Feb. 2020.

[48] H. Wei, S. Zhao, Q. Rong, and H. Bao, "Predicting the effective thermal conductivities of composite materials and porous media by machine learning methods," *Int. J. Heat Mass Transf.*, vol. 127, pp. 908–916, Dec. 2018.

[49] H. H. Hoang and H. H. Trinh, "Improvement for convolutional neural networks in image classification using long skip connection," *Appl. Sci.*, vol. 11, no. 5, p. 2092, Feb. 2021.

[50] M. Yang, X. Li, J. Yuan, Z. Wen, and G. Kang, "A comprehensive study on the effective thermal conductivity of random hybrid polymer composites," *Int. J. Heat Mass Transf.*, vol. 182, Jan. 2022, Art. no. 121936.

[51] Y. Zhang and P. E. Bagnoli, "A modeling methodology for thermal analysis of the PCB structure," *Microelectron. J.*, vol. 45, no. 8, pp. 1033–1052, Aug. 2014.

[52] X. Liu, B. Peng, and W. Yu, "Multiscale modeling of the effective thermal conductivity of 2D woven composites by mechanics of structure genome and neural networks," *Int. J. Heat Mass Transf.*, vol. 179, Nov. 2021, Art. no. 121673.

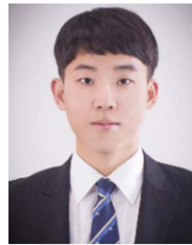

TAE-HYUN KIM received the B.S. degree from the School of Mechanical and Control Engineering, Handong Global University, Pohang, Republic of Korea, in 2019, and the integrated M.S. and Ph.D. degree from the Department of Smart Fab Technology, Sungkyunkwan University, Suwon, Republic of Korea. His research interests include additive manufacturing (3-D print), continuum mechanics, and multiphysics simulation.

JEONG-HYEON PARK received the integrated M.S and Ph.D. degree from the Department of Mechanical Engineering, Sungkyunkwan University, Suwon, Republic of Korea. His research interests include deep learning, computer-aided simulation, and semiconductor package.

KI WOOK JUNG received the M.S. and Ph.D. degrees from the Department of Mechanical Engineering, Stanford University. He is a Staff Thermal Engineer with the Division of Test and System Package, Samsung Electronics. His research interests include heat transfer and semiconductor package.

JAECHOON KIM received the M.S. and Ph.D. degrees from the Department of Mechanical Engineering, Korea University. He is currently a Project Leader in test and system package with the Division of Samsung Electronics. His research interests include heat transfer and semiconductor package.

EUN-HO LEE received the Ph.D. degree from the Department of Mechanical Engineering, KAIST. He has been studying the theory of mechanics for scientific studies and engineering applications. He is a Faculty Member with the School of Mechanical Engineering, Sungkyunkwan University.